

## QUANTUM SIMULATION

# Spin transport in a Mott insulator of ultracold fermions

Matthew A. Nichols<sup>1,2,3</sup>, Lawrence W. Cheuk<sup>2,4</sup>, Melih Okan<sup>1,2,3</sup>, Thomas R. Hartke<sup>1,2,3</sup>, Enrique Mendez<sup>1,2,3</sup>, T. Senthil<sup>1</sup>, Ehsan Khatami<sup>5</sup>, Hao Zhang<sup>1,2,3</sup>, Martin W. Zwierlein<sup>1,2,3\*</sup>

Strongly correlated materials are expected to feature unconventional transport properties, such that charge, spin, and heat conduction are potentially independent probes of the dynamics. In contrast to charge transport, the measurement of spin transport in such materials is highly challenging. We observed spin conduction and diffusion in a system of ultracold fermionic atoms that realizes the half-filled Fermi-Hubbard model. For strong interactions, spin diffusion is driven by super-exchange and doublon-hole-assisted tunneling, and strongly violates the quantum limit of charge diffusion. The technique developed in this work can be extended to finite doping, which can shed light on the complex interplay between spin and charge in the Hubbard model.

In materials, electrons are the elementary carriers of both spin and charge, and one might thus expect that the properties of spin and charge conduction are always closely related. However, strong electron correlations can lead to the separation of charge and spin degrees of freedom, such as in one-dimensional systems (1–3). The unusual transport properties of the cuprate high-temperature superconductors in the normal state have been proposed to arise from decoupled spin and charge transport (4, 5). The simplest model believed to capture the essential features of the cuprate phase diagram, the Fermi-Hubbard model, features spin-charge separation in one dimension (6). In two dimensions, relevant for the cuprates, strong correlations render calculations of transport properties highly challenging (7–13). Simultaneous measurements of transport in both the charge and spin sectors would thus be of great relevance. However, in the cuprates, creating and manipulating spin currents is difficult.

Cold-atom quantum simulators can be used to experimentally study the Fermi-Hubbard model in a pristine, isolated environment, with full control of all Hubbard parameters (14). The advent of quantum gas microscopes for fermionic atoms (15–20), with their single-atom, single-lattice site resolution, has enabled precision measurements of the equation of state (21, 22) and of spin and charge correlations (23–25) of the two-dimensional (2D) Fermi-Hubbard model. These microscopes are poised for the study of transport, as already demonstrated with bosonic atoms (26–31). Previ-

ous measurements of fermionic charge transport were performed without the aid of single-atom resolution (32–34). However, it has proven difficult to directly connect the observed dynamics of lattice systems to the transport coefficients of the underlying Hamiltonian. Recently, the optical charge conductivity of a dilute, harmonically trapped 3D Fermi-Hubbard system has been measured (35), as well as the charge conductance through a mesoscopic lattice in a wire geometry (36).

Here, we explored spin transport in the repulsive 2D Fermi-Hubbard model using ultracold fermionic <sup>40</sup>K atoms on a square lattice confined by a uniform box potential. A natural region in the Hubbard phase diagram where spin and charge transport could differ is near the Mott insulator at half-filling, where charge transport is strongly suppressed, whereas spin transport can occur via super-exchange. Previous experiments have studied spin transport in strongly interacting Fermi gases without a lattice, both in three dimensions (37–40) and in two dimensions (41, 42). In those studies, spin diffusion was observed to attain the quantum limit of  $\sim \hbar/m$ , where  $\hbar$  is Planck's constant  $h$  divided by  $2\pi$  and  $m$  is the particle mass. Here, we measure both the spin diffusion coefficient  $D_S$  and the spin conductivity  $\sigma_S$ . These transport coefficients dictate the response of the system to a spin-dependent force and are related through the Einstein relation,  $\sigma_S = D_S \chi$ , where  $\chi$  is the uniform spin susceptibility, which can be measured independently.

The 2D Fermi-Hubbard model is realized by evaporatively cooling <sup>40</sup>K atoms to quantum degeneracy and preparing them in an equal mixture of the hyperfine states  $|\uparrow\rangle \equiv |F = 9/2, m_F = -3/2\rangle$  and  $|\downarrow\rangle \equiv |F = 9/2, m_F = 1/2\rangle$  in a single layer of a highly oblate optical dipole trap (43). A sample with uniform filling is produced by projecting a repulsive optical potential through the microscope objective (Fig. 1A), which isolates a uniform  $22 \times 22$  site region of the system (44). The sample is subsequently prepared adiabatically

in a square optical lattice, where it is described by the single-band Hubbard Hamiltonian

$$\begin{aligned} \hat{H} = & -t \sum_{\langle i,j \rangle, \sigma} (\hat{c}_{\sigma,i}^\dagger \hat{c}_{\sigma,j} + \text{h.c.}) + \\ & U \sum_i \hat{n}_{\uparrow,i} \hat{n}_{\downarrow,i} - \mu_\uparrow \sum_i \hat{n}_{\uparrow,i} \\ & - \mu_\downarrow \sum_i \hat{n}_{\downarrow,i} + \Delta_\uparrow \sum_i i_x \hat{n}_{\uparrow,i} \\ & + \Delta_\downarrow \sum_i i_x \hat{n}_{\downarrow,i} \end{aligned} \quad (1)$$

Here,  $t$  and  $U$  denote the nearest-neighbor tunneling amplitude and on-site interaction energy, respectively;  $\langle i,j \rangle$  represents nearest-neighbor sites  $i$  and  $j$ ;  $\mu_\uparrow$  ( $\mu_\downarrow$ ) is the chemical potential of atoms in state  $|\uparrow\rangle$  ( $|\downarrow\rangle$ );  $i_x$  represents the  $x$ -coordinate of lattice site  $i$ ; and  $\Delta_\uparrow$  ( $\Delta_\downarrow$ ) represents a possible spin-dependent tilt of the potential along the  $x$ -direction for state  $|\uparrow\rangle$  ( $|\downarrow\rangle$ ). The operators  $\hat{c}_{\sigma,i}^\dagger$  ( $\hat{c}_{\sigma,i}$ ) are the fermion creation (annihilation) operators for spin  $\sigma = \uparrow, \downarrow$  on lattice site  $i$ , and  $\hat{n}_{\sigma,i} = \hat{c}_{\sigma,i}^\dagger \hat{c}_{\sigma,i}$  is the number operator on site  $i$ . To measure the spin transport coefficients  $\sigma_S$  and  $D_S$  at half-filling, we apply a spin-dependent force derived from a magnetic gradient along  $-\hat{x}$  (Fig. 1A). The magnetic gradient gives rise to a linear tilt in the potential energy of  $\Delta_\uparrow/\hbar = 41.1 (\pm 0.8)$  Hz per site and  $\Delta_\downarrow/\hbar = 15.4 (\pm 0.3)$  Hz per site. This tilt has the same sign for atoms of both spins but differs in magnitude. The Hubbard parameters  $t$  and  $U$  have typical values given by  $t/\hbar \sim 100$  Hz and  $U/\hbar \sim 1$  kHz, and their ratio is varied using the depth of the optical lattice.

We first measure the spin diffusion coefficient by preparing the sample adiabatically in the presence of the magnetic gradient. The equilibrium density profile can be understood through the local density approximation (LDA). Under LDA, the local chemical potential  $\mu_{\sigma,j}$  decreases linearly along the  $x$ -direction with slope  $\Delta_\sigma$ , for  $\sigma = \uparrow, \downarrow$ . For a weakly interacting system, one expects the densities of both spins to decrease monotonically along  $\hat{x}$ . This is observed in fluorescence images of samples below and above half-filling, shown in Fig. 1, B and D, respectively. In Fig. 1D, doubly occupied sites appear as holes because of light-assisted collisions during the imaging process (45), so that the left side of the box region, where the density is highest, appears empty. At half-filling, however, the large charge gap of order  $U$  present in the Mott-insulating regime suppresses the formation of double occupancies as long as  $\Delta_{\uparrow,\downarrow} \ll U$ , so that the average density remains homogeneous throughout the sample (Fig. 1, C and E). This directly demonstrates the incompressibility of the Mott-insulating state, which, in an isolated system, suppresses the transport of charge. Spin transport, on the other hand, is not impeded, as spins are free to move.

Indeed, although the total density is insensitive to position, the individual spin densities reveal the effect of the gradient. As shown in Fig. 1E, as well as through images of the individual

<sup>1</sup>Department of Physics, Massachusetts Institute of Technology, Cambridge, MA 02139, USA. <sup>2</sup>MIT-Harvard Center for Ultracold Atoms, Cambridge, MA 02139, USA. <sup>3</sup>Research Laboratory of Electronics, Massachusetts Institute of Technology, Cambridge, MA 02139, USA. <sup>4</sup>Department of Physics, Harvard University, Cambridge, MA 02138, USA. <sup>5</sup>Department of Physics and Astronomy, San José State University, San José, CA 95192, USA.

\*Corresponding author. Email: zwierlein@mit.edu

spin states in Fig. 1, F to H, we observe that  $|\uparrow\rangle$  spins accumulate toward  $-\hat{x}$ , whereas  $|\downarrow\rangle$  spins accumulate toward  $+\hat{x}$  (46). The incompressibility of the Mott insulator forces  $|\downarrow\rangle$  spins to occupy the right half of the sample at the expense of an increase in potential energy due to the tilt. The thermodynamic properties, in-

cluding individual spin densities and double occupancies, of such a tilted fermionic Hubbard system have been studied theoretically using determinant quantum Monte Carlo (DQMC) for weak to intermediate interactions ( $0.08 < t/U < 1$ ) and gradient strengths comparable to those used in the present work (47). Experimentally, we use

this separation of the individual spin densities to measure the entropy of the sample; that is, from the equilibrated total spin density profile  $\langle \hat{S}_{z,j} \rangle = (1/2)\langle \hat{n}_{\uparrow,j} - \hat{n}_{\downarrow,j} \rangle$  in the tilted potential (we retain only the site index along  $\hat{x}$ ), we can obtain the uniform spin susceptibility  $\chi = \partial \langle \hat{S}_{z,j} \rangle / \partial \Delta\mu$ , where  $\Delta\mu = \mu_{\uparrow} - \mu_{\downarrow}$ , of the unperturbed system in linear

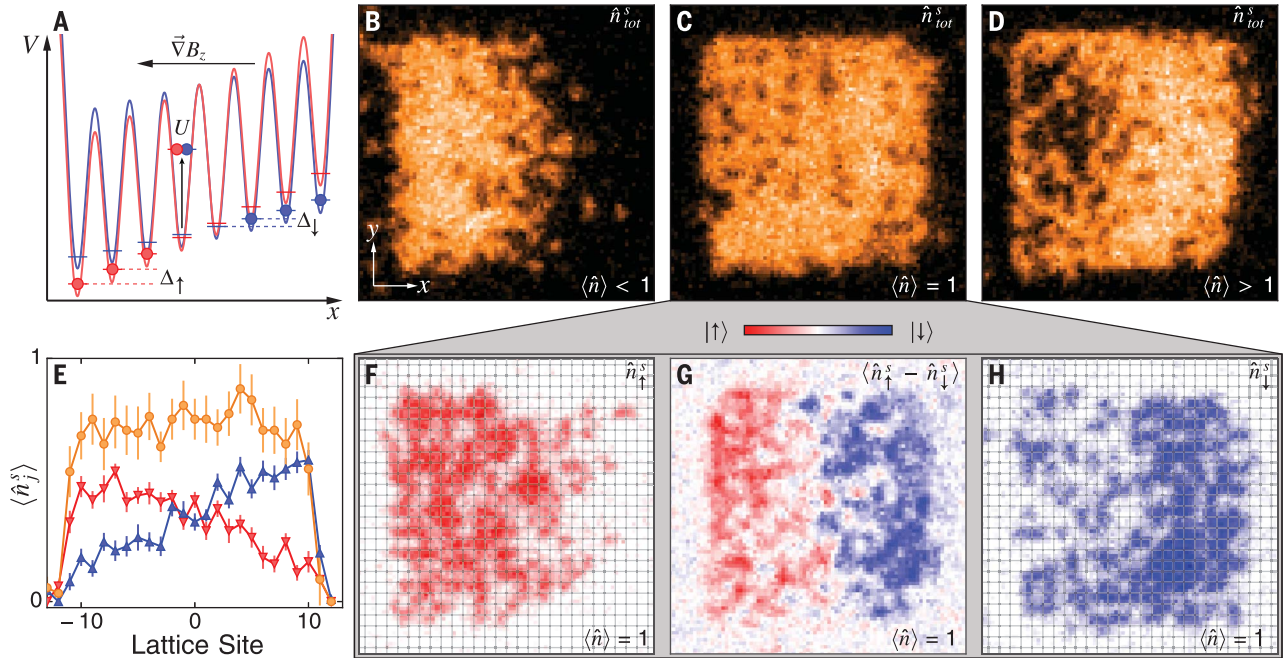


**Fig. 1. Creating spin textures in a homogeneous Fermi-Hubbard system.**

(A) A diagram of the optical potentials used to confine the atoms, and the tilted lattice potential experienced by the two spin states  $|\uparrow\rangle$  (red) and  $|\downarrow\rangle$  (blue) in the presence of a magnetic field gradient. (B to D) Raw fluorescence images of the parity-projected total density  $\hat{n}_{\text{tot}}^s$  for total densities  $\langle \hat{n} \rangle < 1$ ,  $\langle \hat{n} \rangle = 1$ , and  $\langle \hat{n} \rangle > 1$ , respectively, which have been prepared adiabatically in the presence of the magnetic gradient;  $t/U = 0.114 (\pm 0.007)$ ,  $0.067 (\pm 0.004)$ , and  $0.114 (\pm 0.007)$  for (B), (C), and (D), respectively. (E) The average singles

densities,  $\langle \hat{n}_{\text{tot},j}^s \rangle$  (gold),  $\langle \hat{n}_{\uparrow,j}^s \rangle$  (red), and  $\langle \hat{n}_{\downarrow,j}^s \rangle$  (blue) over four independent realizations at  $t/U = 0.026 (\pm 0.002)$ , averaged along the  $y$ -direction from the reconstructed detected site occupations. Error bars represent  $1\sigma$  statistical uncertainty. The average singles densities shown have not been corrected for finite detection fidelity. (F) A single raw image of  $\hat{n}_{\uparrow}^s$  at  $t/U = 0.067 (\pm 0.004)$ . (G) Fluorescence of  $|\uparrow\rangle$  minus fluorescence of  $|\downarrow\rangle$  averaged over six images for the same configuration as (F). (H) A single image of  $\hat{n}_{\downarrow}^s$  for the same configuration as (F).

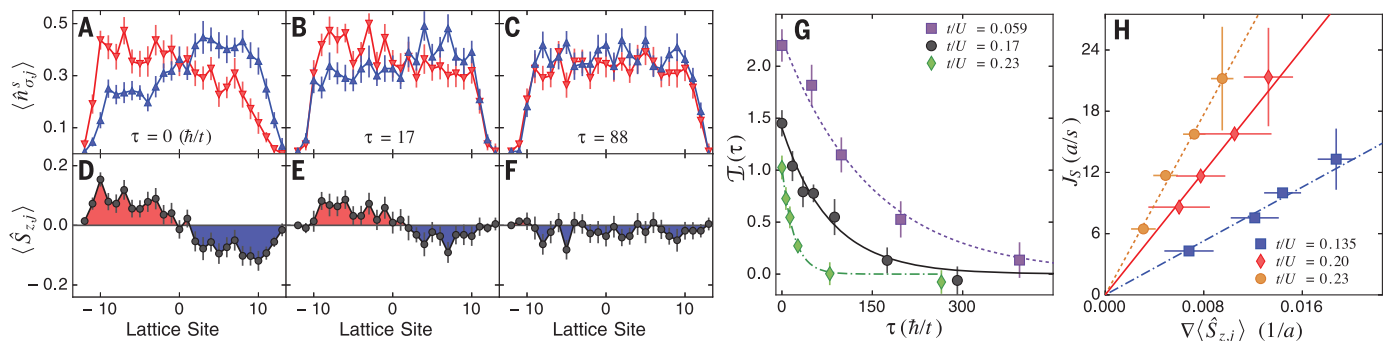


**Fig. 2. Observation of spin relaxation after sudden gradient removal.**

(A to F) Time evolution of the average singles densities  $\langle \hat{n}_{\uparrow,j}^s(\tau) \rangle$  (red) and  $\langle \hat{n}_{\downarrow,j}^s(\tau) \rangle$  (blue) (upper panels), and of the spin density  $\langle \hat{S}_{z,j}(\tau) \rangle$  (lower panels), after removing the magnetic field gradient for  $t/U = 0.23 (\pm 0.01)$  at times  $\tau/\hbar t = 0, 17$ , and  $88$ . (G) Imbalance  $\mathcal{I}(\tau)$  for  $t/U = 0.059 (\pm 0.005)$ ,  $t/U = 0.17 (\pm 0.01)$ , and  $t/U = 0.23 (\pm 0.01)$  and exponential fits to the data. All error bars in (A) to (G) represent  $1\sigma$  statistical uncertainty. (H) Spin current  $J_s$  at  $j = 0$

as a function of the spatial gradient in  $\langle \hat{S}_{z,j}(\tau) \rangle$  at  $j = 0$  for  $t/U = 0.135 (\pm 0.009)$ ,  $t/U = 0.20 (\pm 0.01)$ , and  $t/U = 0.23 (\pm 0.01)$  and corresponding linear fits to the data. The error bars along the horizontal axis represent  $1\sigma$  statistical uncertainty in the measurement of the spatial gradient in  $\langle \hat{S}_{z,j}(\tau) \rangle$ . Vertical error bars are representative for each curve, derived from the uncertainty in the exponential fit to the imbalance  $\mathcal{I}(\tau)$ , and are proportional to the magnitude of the spin current. The data in (A) to (H) have not been corrected for finite detection fidelity.

response (44). By comparing the measured values of  $\chi$  with calculations from the numerical linked-cluster expansion (NLCE) technique (48), we can determine the entropy per particle  $S/k_B N$  (where  $k_B$  is the Boltzmann constant). We find an entropy per particle of  $S/k_B N = 1.1 (\pm 0.1)$ , a regime where NLCE is expected to converge at half-filling over the range of  $t/U$  explored here (23, 49, 50).

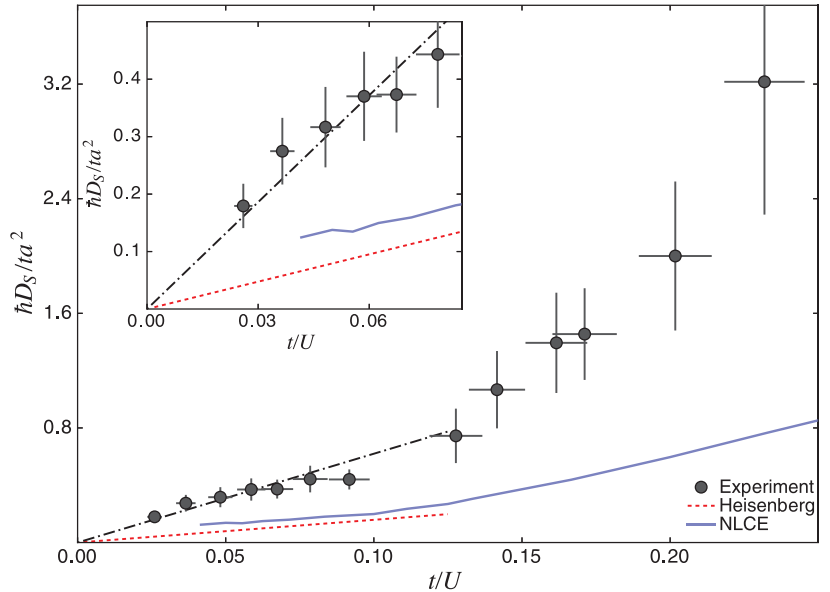
The equilibrated samples with a spin density gradient provide the starting point for subsequent measurements. Because the initial spin density gradient is small, it acts as a small perturbation to the untilted scenario, ensuring that we are probing properties of the homogeneous system in linear response. After the sample has been prepared at a fixed value of  $t/U$ , the magnetic gradient is suddenly switched off. Following this quench, the system begins to relax back to equilibrium, where  $\langle \hat{S}_{z,j} \rangle = 0$  everywhere. Figure 2, A to F, shows the decay of the spin density gradient after the quench for  $t/U = 0.23 (\pm 0.01)$ . This relaxation implies that a spin current  $J_S$  must be present. To obtain  $J_S$  from the measured spin profiles, we define the spin density imbalance,  $\mathcal{I}(\tau)$ , at time  $\tau$  after the quench as

$$\mathcal{I}(\tau) = \sum_L \langle \hat{S}_{z,j}(\tau) \rangle - \sum_R \langle \hat{S}_{z,j}(\tau) \rangle \quad (2)$$

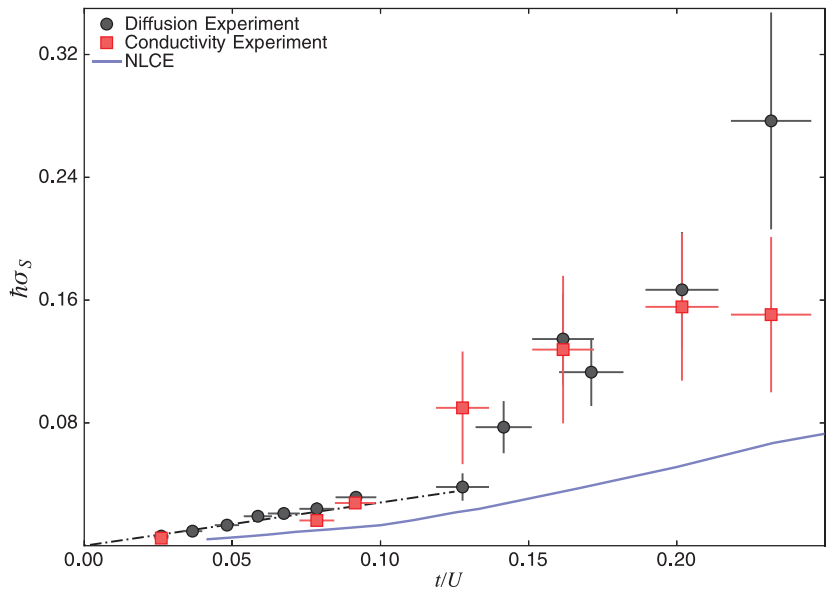
where  $\sum_{L,R}$  denotes summation over the left and right halves of the box. Using the continuity equation for the spin density, one can relate  $\mathcal{I}(\tau)$  to the spin current  $J_S$  at the center of the box ( $j = 0$ ) via  $J_S(\tau) = -(a/2)(d/dt)\mathcal{I}(\tau)$ , where  $a$  is the lattice spacing.

Figure 2G shows  $\mathcal{I}(\tau)$  measured for several values of  $t/U$ . For all values of  $t/U$  explored,  $\mathcal{I}(\tau)$  decays to zero. We have verified that the effects of lattice heating during this decay are negligible relative to the experimental uncertainty in the measurement (44).  $\mathcal{I}(\tau)$  is then fitted to an exponential curve, and the spin current  $J_S$  is obtained through the time derivative of the fit. To connect  $J_S$  with the spin transport coefficients, we first examine the dependence of  $J_S$  on the spin density gradient at the center of the box,  $\nabla \langle \hat{S}_{z,j=0} \rangle$ . By extracting both quantities for a fixed  $t/U$  at various times  $\tau$ , we have access to the dependence of  $J_S$  on  $\nabla \langle \hat{S}_{z,j=0} \rangle$  over a large range of values (Fig. 2H). We find that to within experimental error,  $J_S$  is linearly proportional to  $\nabla \langle \hat{S}_{z,j=0} \rangle$ . This implies that the spin dynamics are diffusive, so that  $J_S = D_S \nabla \langle \hat{S}_{z,j=0} \rangle$ , where  $D_S$  is the spin diffusion coefficient. The diffusive nature of the dynamics is also independently probed by a measurement of the power-law dependence of the decay time of  $\mathcal{I}(\tau)$ , at a fixed value of  $t/U$ , on the system size  $L$  (44).

Figure 3 shows the measured spin diffusion coefficient  $D_S$  of the half-filled, homogeneous Hubbard model as a function of  $t/U$ , in units of the quantum scale for mass diffusion  $D_0 = \hbar/m$ , where  $m = \hbar^2/ta^2$  is the effective mass in the tight-binding limit. For all data in the strongly interacting regime ( $t/U \leq 0.125$ ), the spin diffusion coefficient lies below the scale of quantum-limited mass diffusion  $D_0$ . In this range, the dependence



**Fig. 3. Spin diffusion coefficient of the half-filled Fermi-Hubbard system versus  $t/U$ .** The experimentally measured spin diffusion coefficient  $\hbar D_S/ta^2 \equiv D_S/D_0$  at half-filling (black circles) versus the Hubbard parameters  $t/U$ , and a linear fit to data points with  $t/U < 0.09$  (black dot-dashed line). The vertical error bars represent the  $1\sigma$  statistical error in the measurement; the horizontal error bars represent the  $1\sigma$  statistical error in the calibrated value of  $t/U$ . The blue solid line represents isentropic results for  $D_S/D_0$  obtained from NLCE calculations of the real-time spin current-current correlation function for the Hubbard model (44), with an entropy per particle of  $1.1k_B$ . With a finite temporal cutoff of  $\sim \hbar/t$  for the real-time correlation functions, the NLCE theory is expected to provide a lower bound to the true diffusivity. For comparison, a prediction for the spin diffusion coefficient of the 2D Heisenberg model at high temperatures,  $k_B T \gg J_{\text{ex}}$ , where  $T$  is the temperature, is shown (dashed red line) (8, 51, 52). Inset: A close-up view of the spin diffusion coefficient at half-filling for  $t/U < 0.09$ , where it is expected to scale approximately linearly with  $t^2/U$ .



**Fig. 4. Spin conductivity of the half-filled Fermi-Hubbard system versus  $t/U$ .** The measured spin conductivity at half-filling from the initial spin current in an applied magnetic gradient (red squares) and from the measured spin diffusion coefficient using the Einstein relation  $\sigma_S = D_S \chi$  (black circles). A linear fit to data points with  $t/U < 0.09$  is represented by the black dot-dashed line. The vertical error bars represent the  $1\sigma$  statistical uncertainty of the measurements; the horizontal error bars represent the  $1\sigma$  statistical error in the calibrated value of  $t/U$ . The data have been corrected for finite detection fidelity associated with the imaging process of the two spin states (44). The blue solid line is the result obtained for  $\hbar \sigma_S$  at constant entropy using an NLCE calculation of the real-time spin current-current correlation function for the Hubbard model, with an entropy per particle of  $1.1k_B$  (44).



of  $D_S/D_0$  on  $t/U$  is linear, implying  $D_S \propto t^2/U$ . From a linear fit constrained to go to zero diffusion at  $t/U = 0$  (Fig. 3), we obtain  $\hbar D_S = 6.2 (\pm 0.5) \times a^2 t^2/U$ . This  $t^2/U$  scaling can be partially understood by considering the Heisenberg limit of the half-filled Fermi-Hubbard model, where spins interact with an exchange coupling  $J_{\text{ex}} = 4t^2/U$  called the super-exchange energy. Because  $J_{\text{ex}}$  sets the energy scale in this limit, the effective spin mass is given by  $m_S \sim \hbar^2/J_{\text{ex}}a^2 \sim mU/t$  (29). Spin excitations are thus parametrically more massive than  $m$ . For quantum-limited transport, the spin diffusion coefficient  $D_S$  is given by  $\hbar/m_S$ , giving rise to the  $t^2/U$  scaling. Although this argument gives the correct scaling, the Heisenberg prediction for the spin diffusion coefficient at temperatures much larger than  $J_{\text{ex}}$  is

$$\hbar D_S = \frac{4\sqrt{\pi/20}a^2t^2}{U} \approx \frac{1.6a^2t^2}{U} \quad (3)$$

(8, 51, 52), lower than experimentally observed (Fig. 3). This is not surprising, as the Heisenberg model does not capture quantum or thermal doublon-hole fluctuations of the Fermi-Hubbard model, which arise from states with energies greater than  $U$  (9). Doublon-hole fluctuations can increase spin diffusion because spins can move directly from occupied to empty sites, or can trade places with doublons; both processes occur at a rate set by  $t$ . Because doublon-hole fluctuations are admixed into the wave function of the system with an amplitude proportional to  $t/U$  in the strongly interacting regime, the overall scaling of this mechanism is again proportional to  $t^2/U$ . As shown in Fig. 3, for weaker interaction strengths ( $t/U > 0.125$ ), the diffusivity  $D_S/D_0$  increases faster with  $t/U$  than what is given by this initial linear slope.

To gain further insight, we developed a method to calculate the spin conductivity and diffusivity through real-time current-current correlation functions within the NLCE technique (44). This method avoids the ill-posed problem of analytic continuation from imaginary time, as required in DQMC, and is immune to finite-size effects. These calculations thus give unbiased estimates of transport coefficients in the thermodynamic limit. When comparing the experimental data to the calculations, the only fixed parameter is the entropy per particle, which is independently determined from the measured uniform spin susceptibility. As shown in Fig. 3, the theoretical estimate of the spin diffusivity (blue curve) captures the essential behavior of the experimental data as a function of  $t/U$ . However, the theoretical calculations systematically underestimate the experimental diffusion coefficient. One possible source of this discrepancy arises from limited access to real-time correlation functions for times longer than  $\sim \hbar/t$ . In practice, a cutoff on the order of  $\sim \hbar/t$  is used when calculating the direct current (DC) transport coefficients, which can lead to systematic errors. For example, in the Heisenberg limit, one expects real-time correlations to extend out to times  $\sim \hbar/J_{\text{ex}}$ , which can be much longer

than  $\hbar/t$ . It is therefore notable that even with access to real-time correlations only up to times  $\sim \hbar/t$ , the NLCE estimates agree qualitatively with the experimental data, and also quantitatively to within a factor of  $\sim 2$ . Although it is difficult to estimate the magnitude of the systematic error, we expect the NLCE estimates to provide a lower bound for  $D_S$  (44).

In addition to the spin diffusion coefficient  $D_S$ , we also independently measure the spin conductivity  $\sigma_S$ . To do this, we first prepare an equilibrated system at half-filling without a potential tilt. We then switch on the tilt suddenly, which induces a spin current in the system. Because  $\nabla \langle \hat{S}_{z,j} \rangle = 0$  at time  $\tau = 0$ , the diffusive contribution to the spin current is negligible initially; in analogy with Ohm's law, which relates a charge current to an applied electric field using the charge conductivity, the initial spin current  $J_S$  ( $\tau = 0$ ) is directly proportional to the applied spin-dependent force,  $-(1/a)(\Delta_{\uparrow} - \Delta_{\downarrow})\hat{x}$ , where the spin conductivity  $\sigma_S$  is the constant of proportionality. Therefore, by measuring the spin current at the center of the box under the known spin-dependent tilt, the spin conductivity can be obtained. The measured spin conductivities at various interaction strengths  $t/U$  are shown in Fig. 4. A second way to obtain the conductivity is through the Einstein relation  $\sigma_S = D_S\chi$ , where the spin diffusion coefficient  $D_S$  and the uniform spin susceptibility  $\chi$  are both obtained from the data used in Fig. 3. The values of  $\hbar\sigma_S$  obtained in this way are also shown in Fig. 4. We find that these two independent methods of measuring the spin conductivity agree with each other to within experimental uncertainty.

We observe that the spin conductivity is linear with  $t/U$  in the strongly interacting regime ( $t/U \leq 0.125$ ), and find that  $\sigma_S = 0.28 (\pm 0.02) \times t/U\hbar$  from a linear fit constrained to yield zero conductivity at  $t/U = 0$  (Fig. 4). The measured spin conductivities drop far below the Mott-Ioffe-Regel limit for charge in a metal (53, 54),  $\sigma_0 = ne^2\tau/m = e^2/\hbar$ , derived for a scattering rate  $\tau^{-1} = E_F/\hbar$  given by the Fermi energy  $E_F$ , where the elementary charge of our system is  $e = 1$ . It therefore appears once again as if the effective mass of the carriers of spin is  $m_S \sim mU/t$ . A breakdown of the Mott-Ioffe-Regel limit is naturally expected in our regime where quasiparticles are ill-defined and Drude-Boltzmann theory does not apply. As  $t/U$  increases, the observed spin conductivity grows beyond the initial linear scaling with  $t/U$ , in analogy with the diffusion coefficient. NLCE predictions for  $\hbar\sigma_S$  at half-filling (blue curve in Fig. 4) capture the behavior of the spin conductivity with  $t/U$  qualitatively, but are systematically lower than the experimental data, for the same potential reasons discussed previously in the context of the diffusion coefficient. Given the substantial challenges associated with calculating the DC limit of the spin conductivity, the experimental data provide a valuable benchmark for future theoretical calculations.

Our study of spin transport can be readily extended in many ways. For example, one can

explore the temperature dependence of the spin resistivity, which could display linear behavior reminiscent of charge transport in bad metals. One can also investigate the effect of doping away from half-filling (e.g., at optimal doping), where superconducting fluctuations or a strange metal phase could be present in experimentally attainable conditions. Through simultaneous measurements of both the spin and charge dynamics, such experiments could elucidate the intricate interplay between these two degrees of freedom in the Fermi-Hubbard model.

## REFERENCES AND NOTES

1. T. Giamarchi, *Quantum Physics in One Dimension* (Clarendon, 2004).
2. O. M. Auslaender et al., *Science* **308**, 88–92 (2005).
3. A. J. Heeger, S. Kivelson, J. R. Schrieffer, W. P. Su, *Rev. Mod. Phys.* **60**, 781–850 (1988).
4. P. W. Anderson, *Phys. Today* **50**, 42–47 (1997).
5. P. A. Lee, N. Nagaosa, X.-G. Wen, *Rev. Mod. Phys.* **78**, 17–85 (2006).
6. E. H. Lieb, F. Y. Wu, *Phys. Rev. Lett.* **20**, 1445–1448 (1968).
7. D. J. Scalapino, S. R. White, S. Zhang, *Phys. Rev. B* **47**, 7995–8007 (1993).
8. J. Bonča, J. Jaklič, *Phys. Rev. B* **51**, 16083–16087 (1995).
9. P. Kopietz, *Phys. Rev. B* **57**, 7829–7834 (1998).
10. S. Mukerjee, V. Oganesyan, D. Huse, *Phys. Rev. B* **73**, 035113 (2006).
11. H. Kim, D. A. Huse, *Phys. Rev. A* **86**, 053607 (2012).
12. A. P. Snyder, T. N. De Silva, *Phys. Rev. A* **86**, 053610 (2012).
13. C. Karrasch, D. M. Kennes, J. E. Moore, *Phys. Rev. B* **90**, 155104 (2014).
14. T. Esslinger, *Annu. Rev. Condens. Matter Phys.* **1**, 129–152 (2010).
15. L. W. Cheuk et al., *Phys. Rev. Lett.* **114**, 193001 (2015).
16. E. Haller et al., *Nat. Phys.* **11**, 738–742 (2015).
17. M. F. Parsons et al., *Phys. Rev. Lett.* **114**, 213002 (2015).
18. A. Omran et al., *Phys. Rev. Lett.* **115**, 263001 (2015).
19. G. J. A. Edge et al., *Phys. Rev. A* **92**, 063406 (2015).
20. P. T. Brown et al., *Science* **357**, 1385–1388 (2017).
21. E. Cocchi et al., *Phys. Rev. Lett.* **116**, 175301 (2016).
22. C. Hofrichter et al., *Phys. Rev. X* **6**, 021030 (2016).
23. L. W. Cheuk et al., *Science* **353**, 1260–1264 (2016).
24. M. Boll et al., *Science* **353**, 1257–1260 (2016).
25. M. F. Parsons et al., *Science* **353**, 1253–1256 (2016).
26. M. Cheneau et al., *Nature* **481**, 484–487 (2012).
27. T. Fukuhara et al., *Nat. Phys.* **9**, 235–241 (2013).
28. T. Fukuhara et al., *Nature* **502**, 76–79 (2013).
29. S. Hild et al., *Phys. Rev. Lett.* **113**, 147205 (2014).
30. P. M. Preiss et al., *Science* **347**, 1229–1233 (2015).
31. J. Y. Choi et al., *Science* **352**, 1547–1552 (2016).
32. N. Strohmaier et al., *Phys. Rev. Lett.* **99**, 220601 (2007).
33. U. Schneider et al., *Nat. Phys.* **8**, 213–218 (2012).
34. W. Xu, W. R. McGehee, W. N. Morong, B. DeMarco, arXiv:1606.06669v5 [cond-mat.quant-gas] (28 August 2018).
35. R. Anderson, F. Wang, P. Xu, V. Venu, S. Trotzky, F. Chevy, J. H. Thywissen, arXiv:1712.09965v2 [cond-mat.quant-gas] (28 May 2018).
36. M. Lebrat et al., *Phys. Rev. X* **8**, 011053 (2018).
37. A. Sommer, M. Ku, G. Roati, M. W. Zwierlein, *Nature* **472**, 201–204 (2011).
38. A. Sommer, M. Ku, M. W. Zwierlein, *New J. Phys.* **13**, 055009 (2011).
39. A. B. Bardon et al., *Science* **344**, 722–724 (2014).
40. G. Valtolina et al., *Nat. Phys.* **13**, 704–709 (2017).
41. M. Koschorreck, D. Pertot, E. Vogt, M. Köhl, *Nat. Phys.* **9**, 405–409 (2013).
42. C. Luciuk et al., *Phys. Rev. Lett.* **118**, 130405 (2017).
43. L. W. Cheuk et al., *Phys. Rev. Lett.* **116**, 235301 (2016).
44. See supplementary materials.
45. M. T. DePue, C. McCormick, S. L. Winoto, S. Oliver, D. S. Weiss, *Phys. Rev. Lett.* **82**, 2262–2265 (1999).
46. D. M. Weld et al., *Phys. Rev. Lett.* **103**, 245301 (2009).
47. G. G. Batrouni, R. T. Scalettar, *Phys. Rev. A* **96**, 033632 (2017).
48. M. Rigol, T. Bryant, R. R. P. Singh, *Phys. Rev. Lett.* **97**, 187202 (2006).
49. E. Khatami, M. Rigol, *Phys. Rev. A* **84**, 053611 (2011).
50. E. Khatami, M. Rigol, *Phys. Rev. A* **86**, 023633 (2012).

51. H. S. Bennett, P. C. Martin, *Phys. Rev.* **138**, A608–A617 (1965).
52. A. Sokol, E. Gagliano, S. Bacci, *Phys. Rev. B* **47**, 14646–14649 (1993).
53. A. F. Ioffe, A. R. Regel, *Prog. Semicond.* **4**, 237–291 (1960).
54. N. F. Mott, *Philos. Mag.* **26**, 1015–1026 (1972).
55. M. A. Nichols, Replication data for: Spin transport in a Mott insulator of ultracold fermions. Harvard Dataverse (2018); <https://doi.org/10.7910/DVN/OOFNFY>.

#### ACKNOWLEDGMENTS

We thank W. S. Bakr, M. Greiner, and their research groups for fruitful discussions. **Funding:** Supported by NSF, AFOSR, an AFOSR MURI on Exotic Quantum Phases, ARO, ONR, the David and

Lucile Packard Foundation, and Gordon and Betty Moore Foundation grant GBMF5279. E.K. was supported by NSF grant DMR-1609560. The computations were performed in part on the Teal computer cluster of the Department of Physics and Astronomy of San José State University and in part on the Spartan high-performance computing facility at San José State University supported by NSF grant OAC-1626645. T.S. was supported by NSF grant DMR-1608505 and partially through a Simons Investigator Award from the Simons Foundation. **Author contributions:** M.A.N., L.W.C., M.O., T.R.H., E.M., H.Z., and M.W.Z. planned and performed the experiment and analyzed the data. E.K. performed the NLCE simulations. All authors contributed to the interpretation of the data and the preparation of the manuscript. **Competing**

**interests:** The authors declare no competing financial interests.

**Data and materials availability:** All data shown in this work can be found in an online database (55).

#### SUPPLEMENTARY MATERIALS

[www.sciencemag.org/content/363/6425/383/suppl/DC1](http://www.sciencemag.org/content/363/6425/383/suppl/DC1)  
Supplementary Text  
Figs. S1 to S6  
References (56–61)

26 February 2018; accepted 20 November 2018

Published online 6 December 2018

10.1126/science.aat4387

## Spin transport in a Mott insulator of ultracold fermions

Matthew A. Nichols, Lawrence W. Cheuk, Melih Okan, Thomas R. Hartke, Enrique Mendez, T. Senthil, Ehsan Khatami, Hao Zhang and Martin W. Zwierlein

*Science* **363** (6425), 383-387.

DOI: 10.1126/science.aat4387originally published online December 6, 2018

### Simulating transport with cold atoms

Much can be learned about the nature of a solid from how charge and spin propagate through it. Transport experiments can also be performed in quantum simulators such as cold atom systems, in which individual atoms can be imaged using quantum microscopes. Now, two groups have investigated transport in the so-called Fermi-Hubbard model using a two-dimensional optical lattice filled with one fermionic atom per site (see the Perspective by Brantut). Moving away from half-filling to enable charge transport, Brown *et al.* found that the resistivity had a linear temperature dependence, not unlike that seen in the strange metal phase of cuprate superconductors. In a complementary study on spin transport, Nichols *et al.* observed spin diffusion driven by superexchange coupling.

*Science*, this issue p. 379, p. 383; see also p. 344

#### ARTICLE TOOLS

<http://science.sciencemag.org/content/363/6425/383>

#### SUPPLEMENTARY MATERIALS

<http://science.sciencemag.org/content/suppl/2018/12/05/science.aat4387.DC1>

#### RELATED CONTENT

<http://science.sciencemag.org/content/sci/363/6425/344.full>  
<http://science.sciencemag.org/content/sci/363/6425/379.full>

#### REFERENCES

This article cites 58 articles, 8 of which you can access for free  
<http://science.sciencemag.org/content/363/6425/383#BIBL>

#### PERMISSIONS

<http://www.sciencemag.org/help/reprints-and-permissions>

Use of this article is subject to the [Terms of Service](#)